

# Mixed-halide perovskites solar cells through PbI<sub>2</sub> and PbCl<sub>2</sub> precursor films by sequential chemical vapor deposition

Siphelo Ngqoloda<sup>a,\*</sup>, Christopher J. Arendse<sup>a,b,\*</sup>, Suchismita Guha<sup>a,b</sup>, Theophillus F. Muller<sup>a</sup>, Stephen C. Klue<sup>a</sup>, Siphesihle S. Magubane<sup>a</sup>, Clive J. Oliphant<sup>a,c</sup>

<sup>a</sup> Department of Physics and Astronomy, University of the Western Cape, Private Bag X17, Bellville 7535, South Africa

<sup>b</sup> Department of Physics and Astronomy, University of Missouri, Columbia, MO 65211, United States

<sup>c</sup> Materials Characterization, National Metrology Institute of South Africa, Private Bag X34, Lynnwood Ridge, Pretoria 0040, South Africa

## ARTICLE INFO

### Keywords:

Chlorine doped perovskites  
Lead chloride iodide  
Chemical vapor deposition  
Large grains  
Substitution

## ABSTRACT

Mixed halide perovskites with chlorine (Cl) content have received significant interest due to better charge transport properties and longer diffusion length compared to pure iodine-based perovskites. The superior properties of Cl-doped perovskites improve solar cell device performance, although the quantification of Cl composition in the perovskite films remain difficult to achieve. Hence, it is difficult to correlate the Cl-quantity with the improved device performance. In this work, we deposited Cl-doped perovskite films through a facile three- and two-step sequential chemical vapor deposition (CVD) where lead halide films were deposited in the first steps of the process and subsequently converted to perovskites. No Cl substitution by iodine was observed during a sequential deposition of lead chloride and lead iodide films which reacted to form a lead chloride iodide phase (PbI<sub>2</sub>Cl). The substitution of Cl by iodine ions only occurred during the conversion to perovskite phase. Large perovskite grains (greater than 2 μm) were realized when converting a PbI<sub>2</sub> film to perovskite compared to chlorine containing lead halide films, contradicting literature. However, Cl doped perovskite solar cells showed improved device efficiencies as high as 10.87% compared to an un-doped perovskite solar cell (8.76%).

## 1. Introduction

Organic-inorganic hybrid perovskites are considered one of the most attractive semiconducting materials due to their exceptional optical and electrical properties, including an appropriate bandgap, high absorption coefficient, high mobility of electrons and holes, longer carrier diffusion lengths, lower exciton binding energies, and facile deposition methods (Jena et al., 2019; Swartwout et al., 2019; Wang et al., 2019). Since their first application as light absorbing materials in photovoltaic technology (Kojima et al., 2009), perovskites based solar cells have achieved remarkable progress with certified record power conversion efficiency (PCE) of over 25.2% in just few years (“Best Research-Cell Efficiency Chart | Photovoltaic Research | NREL,” n.d.).

Hybrid perovskites are composed of an organic cation like methyl ammonium (MA<sup>+</sup>), inorganic lead (Pb<sup>2+</sup>), and lastly halide anions (iodine (I<sup>-</sup>), bromide (Br<sup>-</sup>), chlorine (Cl<sup>-</sup>), or mixed halides) (Jena et al., 2019; Swartwout et al., 2019; Wang et al., 2019). There are other combinations that have been used such as replacement of the MA cation

with formamidinium, but the methyl ammonium lead iodide (MAPbI<sub>3</sub>) or mixed halide MAPbI<sub>3-x</sub>Cl<sub>x</sub> perovskites have received wider attention (Ono et al., 2017). Mixed halide perovskites have longer charge carrier diffusion lengths of up to 3 μm compared to its pure iodide based counterparts with diffusion lengths ranging between 0.1 and 1 μm (Ono et al., 2016).

Even though doping hybrid perovskites with chlorine (Cl<sup>-</sup>) ions improves device performance, its role has been largely debated and its incorporation within the perovskite structure has also been doubted (Chae et al., 2015; Ono et al., 2017). It is known that enhanced crystallization of perovskite films with improved grain size occurs when Cl is included in one of the perovskite deposition precursors, such as lead chloride (PbCl<sub>2</sub>) or MA chloride (MACl) (Chae et al., 2015; Fan et al., 2017; Luo et al., 2015b; Wittich et al., 2018; Zhang et al., 2019). The improved crystallization of Cl-doped perovskites is achieved through slow crystal growth compared to the pure iodine based counterparts; this in return suppresses the defect density at the grain boundaries (Richter et al., 2016; Yang et al., 2017, 2016, 2015). These general

\* Corresponding authors at: Department of Physics and Astronomy, University of the Western Cape, Private Bag X17, Bellville 7535, South Africa (C.J. Arendse).  
E-mail addresses: [2807183@myuwc.ac.za](mailto:2807183@myuwc.ac.za) (S. Ngqoloda), [cjarendse@uwc.ac.za](mailto:cjarendse@uwc.ac.za) (C.J. Arendse).

<https://doi.org/10.1016/j.solener.2020.12.042>

Received 30 September 2020; Received in revised form 27 November 2020; Accepted 16 December 2020

Available online 12 January 2021

0038-092X/© 2021 International Solar Energy Society. Published by Elsevier Ltd. All rights reserved.

conclusions mainly relate to perovskite films where the solution method is used at either during single or two step synthesis (Chae et al., 2015; Fan et al., 2017; Luo et al., 2015b; Richter et al., 2016; Wittich et al., 2018; Yang et al., 2017, 2016, 2015; Zhang et al., 2019). The uncertainty about the presence of Cl in perovskite films stems from the difficulty in detecting it through elemental composition characterization techniques such as X-ray photoelectron spectroscopy (XPS) and energy dispersive X-ray spectroscopy (EDS) (Ng et al., 2015; Williams et al., 2014). This difficulty arises because the Cl composition in the films is usually very low and below the detection limit (0.1 at.%) of these characterization techniques (Ono et al., 2017). This low Cl concentration in the films is due to an easy replacement of a smaller Cl<sup>-</sup> ionic radius (1.67 Å) by a larger I<sup>-</sup> ionic radius (2.07 Å) during the perovskite intercalation reaction (Zhang et al., 2019).

There are two main routes for perovskite deposition, namely solution methods where perovskite precursors are dissolved in appropriate solvents, whereas the other method entails vapor deposition from perovskite solid precursors (powders) (Cao et al., 2018; C.-W. Chen et al., 2014; Ha et al., 2014; Leyden et al., 2014; Liu et al., 2013; Luo et al., 2016; Tavakoli et al., 2015; Tombe et al., 2017; Yang et al., 2015; Yu et al., 2014). During spin coating of mixed halide perovskites it is usually required to have a molar ratio of 1:3 for PbCl<sub>2</sub>:MAI in order to achieve better device performance (Cao et al., 2018; Chae et al., 2015; Ono et al., 2017). Another challenge with spin coating is the difficulty in dissolving PbCl<sub>2</sub> in DMF (common solvent) making it difficult to study the as-deposited PbCl<sub>2</sub> before conversion to perovskites (Fan et al., 2017; Ono et al., 2017), as investigated in a series of PbCl<sub>2</sub>:PbI<sub>2</sub> molar ratios dissolved in a blend of DMF and dimethyl sulfoxide (DMSO) during a two-step spin coating. The devices prepared from precursor solution containing more PbCl<sub>2</sub> performed poorly due to poor conversion of thin films to perovskites.

There have been a number of studies on the deposition of PbCl<sub>2</sub> films through high vacuum thermal evaporation (C.-W. Chen et al., 2014; Leyden et al., 2014; Liu et al., 2013; Ng et al., 2015; Yang et al., 2015), with few using low pressure (around 1 mbar) chemical vapor deposition (CVD) (Ha et al., 2014; Tavakoli et al., 2015). Furthermore, low pressure CVD has been employed to prepare perovskite thin films, but mainly during the conversion step from either solution deposited PbI<sub>2</sub> (Luo et al., 2015a; Peng et al., 2015; Shen et al., 2016a, 2016b; Wang and Chen, 2016) or vacuum deposited (thermal evaporation) Pb halide films (Ioakeimidis et al., 2016; Leyden et al., 2016, 2014). Preparation of perovskite films for solar cell devices using two step depositions where Pb halides and the conversion to perovskites are both done in the CVD chamber are very rare (Ngqoloda et al., 2020b; Tran et al., 2018). In essence, the two-step low pressure CVD method offers a simplified scalable route for perovskite deposition using a single CVD chamber.

Therefore, we explore a three-step deposition of mixed halide perovskites through the deposition of PbCl<sub>2</sub> and PbI<sub>2</sub> layers sequentially, using a low-pressure CVD method such that a stable lead chloride iodide (PbI<sub>2</sub>) phase is formed. This route is compared to a two-step deposition of perovskite films where separate layers of PbCl<sub>2</sub> and PbI<sub>2</sub> are deposited individually on separate substrates. These Pb halide films are exposed to MAI vapor as the last step of the three- and two-step deposition for the conversion to perovskite phase where the intercalation reaction takes place between the pre-deposited Pb halides and the MAI molecules. According to available literature, this is a first study where perovskite solar cells are prepared by exposing CVD grown PbI<sub>2</sub> and PbCl<sub>2</sub> films into MAI vapor for conversion to perovskites using the same CVD furnace. It is observed here that during the Pb halide double layer deposition at high substrate temperatures and relatively low pressure there was no substitution of Cl by iodine; instead, a stable PbI<sub>2</sub> phase was formed. However, during the step whereby the chlorine containing films were exposed to the MAI vapor, chlorine was completely replaced by iodine according to our EDS and XPS results, similar to what has been reported before (Ng et al., 2015; Williams et al., 2014).

We observe that converting a PbI<sub>2</sub> film yields large perovskite grains

(average grain size of 1048 nm) compared to converting the PbCl<sub>2</sub> film, which produced perovskites with average grain size of 937 nm. These results contradict the notion that Cl-doping in perovskite leads to improved crystallization and larger grain size (Dong et al., 2015; Richter et al., 2016; Yang et al., 2017, 2016). Our results suggest that the grain size is not the only factor for improving the solar cell efficiency. Planar perovskite solar cell device performance was improved for Cl-doped perovskites with PCE as high as 10.87% compared to its pure iodine-based counterparts with PCE = 8.76%.

## 2. Experimental section

### 2.1. Fabrication of perovskite solar cells

The perovskite solar cells fabrications were all done under fully open air and at ambient room conditions (temperature and relative humidity). A similar fabrication procedure was adopted from our previous reports (Ngqoloda et al., 2020a, 2020b). Chemicals employed here were purchased from Sigma-Aldrich (unless stated) and used as bought. Fluorine-doped tin oxide (FTO) coated on glass substrates (10 Ohms/sq.) were cut into 1.5 cm by 2 cm pieces and etched with Zn powder and 2 M hydrochloric acid (HCl). Samples were cleaned with hellmanex detergent (2%) and then isopropanol in an ultrasonic bath sequentially and followed by a thorough rinsing in hot deionized water then treated under UV Ozone for 15 min. Then, 365 μL of titanium isopropoxide was added into 2.5 ml of ethanol, and 35 μL of HCl (2 M) was added into 2.5 ml of ethanol, mixed and stirred for an hour. The solution was spin coated on etched FTO substrates at 2000 rpm for 30 s; the spin coating was repeated with a 4000 rpm spin speed for 30 s and dried on a hot plate for 5 min. The films were then annealed at 500 °C for 30 min to form a compact titanium dioxide (c-TiO<sub>2</sub>) film (Ngqoloda et al., 2020b).

Lead halide films were prepared by two-step sequential CVD to deposit double halide layers of PbCl<sub>2</sub> and PbI<sub>2</sub> for the formation of lead chloride iodide (PbI<sub>2</sub>), and one-step CVD to deposit single halide layers (PbI<sub>2</sub> and PbCl<sub>2</sub>), respectively. For the deposition of these mixed halides films, first PbCl<sub>2</sub> was deposited (~75 nm thickness) followed by PbI<sub>2</sub> (also ~75 nm) and the sample named PbCl<sub>2</sub>/PbI<sub>2</sub>. For single halide layers, film thicknesses were about 150 nm for both PbI<sub>2</sub> and PbCl<sub>2</sub>. These deposition steps are shown schematically in Fig. 1 together with the conversion to perovskites.

For the Pb halides (PbI<sub>2</sub> or PbCl<sub>2</sub>) deposition about 150 mg of lead (II) iodide powder (99%) or lead (II) chloride powder (98%) were placed inside a three zone tube furnace (Brother XD 1600MT) at the center of the first zone on ceramic boats (Ngqoloda et al., 2020b). Glass/FTO/c-TiO<sub>2</sub> substrates were placed down-stream at optimized temperature dependent positions. The furnace was then pumped down to a base pressure reaching 0.08 mbar and followed by ramping of the source (PbI<sub>2</sub> or PbCl<sub>2</sub>) zones to their respective sublimation temperatures, 380 °C for PbI<sub>2</sub> and 450 °C for PbCl<sub>2</sub>. To prepare the PbI<sub>2</sub> film, about 75 nm thick PbCl<sub>2</sub> was deposited with a substrate temperature of 150 °C, placed downstream at 18 cm away from the source. The thin PbCl<sub>2</sub> sample was exposed to PbI<sub>2</sub> vapor employing substrates temperature of 125 °C (at 17 cm downstream) which would give 75 nm of PbI<sub>2</sub> film; the two compounds reacted to form PbI<sub>2</sub>.

To achieve a 150 nm thick PbI<sub>2</sub> layer a 135 °C nominal substrate temperature was employed with substrates placed at about 16 cm downstream. And finally for 150 nm thick PbCl<sub>2</sub> film the samples were placed at about 17 cm away from the source at a substrate temperature of 160 °C. Dry nitrogen gas (N<sub>2</sub>) was used as a carrier gas to transport Pb halide vapors towards the substrates at a flow rate of 100 sccm. The deposition was carried at a deposition pressure of 300 mbar which was controlled by an automated pressure regulator system. Deposition of Pb halides was allowed to dwell for 40 min and the furnace was allowed to cool down to room temperature.

The perovskite conversion from the Pb halide thin films (last step) was carried in the same furnace with a fresh ceramic tube and following

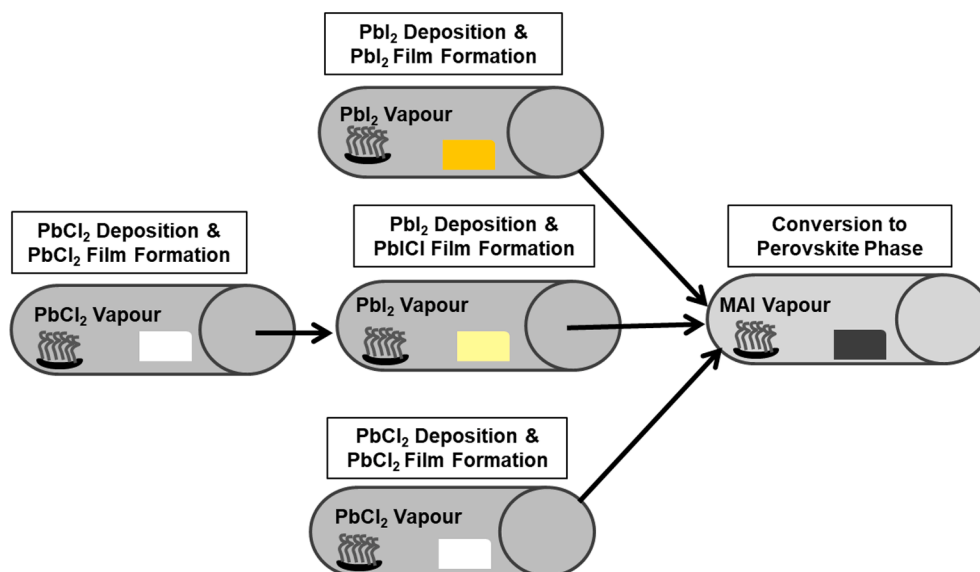


Fig. 1. Schematic representation of the film deposition process during sequential low-pressure CVD method.

a modified conversion method compared to our previous publication (Ngqoloda et al., 2020b). Briefly, about 150 mg of methyl ammonium iodide (MAI) (Dyesol) salt on a fresh ceramic boat was also placed at the center of the furnace first zone. The Pb halide films on Glass/FTO/c-TiO<sub>2</sub> substrates were placed downstream at a distance of 8 cm away from the MAI source. The zone with MAI source was then ramped up to a nominal temperature of 180 °C, and substrates reached a nominal temperature of 130 °C. The conversion of Pb halides to perovskites was allowed for 60 min at a controlled pressure of 10 mbar and N<sub>2</sub> flow rate of 100 sccm. These were our optimized conversion condition where Pb halides fully convert to MAPbI<sub>3</sub> or mixed halide perovskites films. The low pressure (10 mbar) and shorter time (60 min) used in this work compared to our previous publication were based on the new optimum conditions for Cl containing perovskites. The deposition steps schematic is shown in Fig. 1.

The solar cell devices were finalized by depositing a hole transport layer (HTL), spin coated on top of the perovskite film at a spin speed of 2000 rpm 20 s. The HTL solution composed of 80 mg of 2,2'',7,7''-tetrakis(N,N-di-p-methoxyphenylamine)-9,9-spirobifluorene (Spiro-MeO TAD) dissolved in 1 ml of chlorobenzene, where 40 µL of 4-*tert*-butylpyridine (tBP) and 25 µL of lithium bis-(trifluoromethanesulfonyl)imide (LITFSI) solution (52 mg of LITFSI in 100 µL of acetonitrile) were added and the solutions was stirred for 30 min. Lastly, about 100 nm of silver electrode was deposited by thermal evaporation under a pressure of about  $1 \times 10^{-5}$  mbar through a shadow mask which is made of ultrathin stainless steel, with a device active area of 0.0512 cm<sup>2</sup>.

## 2.2. Characterization

The Panalytical Empyrean X-ray diffractometer with Cu K $\alpha$  (1.54 Å) was used to study the phase composition and crystal structure of the films and was operated at an acceleration voltage of 45 kV and a current of 40 mA, scanning over 2 $\theta$  range of 10–100° with a scan step of 0.02°. A Zeiss Auriga field-emission gun Scanning Electron Microscope (FEG-SEM) and a Zeiss Cross Beam 540 focused ion beam scanning electron microscope (FIBSEM), operated at acceleration voltages of 1–5 kV, were used to investigate the morphology of the films. The FIBSEM is equipped with energy dispersive X-ray spectroscopy (EDS) facilities to identify the elemental composition of the samples. To investigate chemical composition of the converted perovskites films, X-ray photoelectron spectroscopy (XPS) was employed, using a Thermo Scientific ESCALAB 250Xi surface analysis instrument, equipped with a monochromatic Al K $\alpha$  X-

ray (1486.7 eV) source. Optical transmission measurements were performed using an Ocean Optics UV–visible spectrophotometer and the spectra were measured from 250 to 1000 nm with spectral resolution of 0.5 nm. Photoluminescence (PL) measurements were performed in reflection geometry using the 457 nm line of an Argon ion laser as the excitation source with the laser power on the sample being < 10 mW. The PL spectra were collected with an Ocean Optics USB Flame Spectrometer. Current density–voltage (J–V) curves were recorded using a Keithley 2420 source meter with an illumination of 100 mW/cm<sup>2</sup>, AM1.5, employing a solar simulator (Sciencetech Inc.) in air. The solar cells were illuminated for 15 s before measurements and were scanned in reverse (1 to –0.2 V) and forward (–0.2 to 1 V) with a step voltage of 12 mV.

## 3. Results and discussion

### 3.1. Structural and morphological properties

The sequential CVD of perovskite films during the three-step and two-step processes is shown schematically in Fig. 1. Pb halide films were formed in the first steps of the deposition process and these films were subsequently converted to perovskites in the final step. Briefly, during the three-step sequential deposition about 75 nm PbCl<sub>2</sub> film was deposited first followed by another 75 nm PbI<sub>2</sub> layer (second step) for the sample named PbCl<sub>2</sub>/PbI<sub>2</sub>. During this route, a stable lead chloride iodide film (PbI<sub>2</sub>) was formed with a total thickness of about 143 nm (measured with a thickness profilometer). For the two-step deposition, in the first step single layers of PbI<sub>2</sub> (sample PbI<sub>2</sub>) and PbCl<sub>2</sub> (sample PbCl<sub>2</sub>) were separately deposited with a thickness of about 150 nm each. The successful deposition of these layers is validated by the X-ray diffraction (XRD) patterns in Fig. 2a deposited on fluorine doped tin oxide (FTO) coated with a thin layer of compact titanium dioxide (c-TiO<sub>2</sub>) thin film.

XRD patterns Fig. 2a shows a crystalline PbI<sub>2</sub> indexed to a hexagonal (*P3m1*) structure (Schieber et al., 2008; Sun et al., 2014) with peaks at ~ 12.74°, 25.59°, and 38.75°, assigned to the (001), (002), and (003) diffracting planes, respectively, according to the Joint Committee on Powder Diffraction Standards (JCPDS, data no. 07–0235). The PbCl<sub>2</sub> film shows XRD peaks (Fig. 2a) at 22.01°, 22.92°, 23.44°, 24.99°, 32.33°, and 40.0° indexed to the (101), (020), (210), (111), (121), and (004) diffracting planes, respectively, (JCPDS, data no. 01–0536) and all belong to the orthorhombic (Pnma) PbCl<sub>2</sub> structure (Costa et al.,

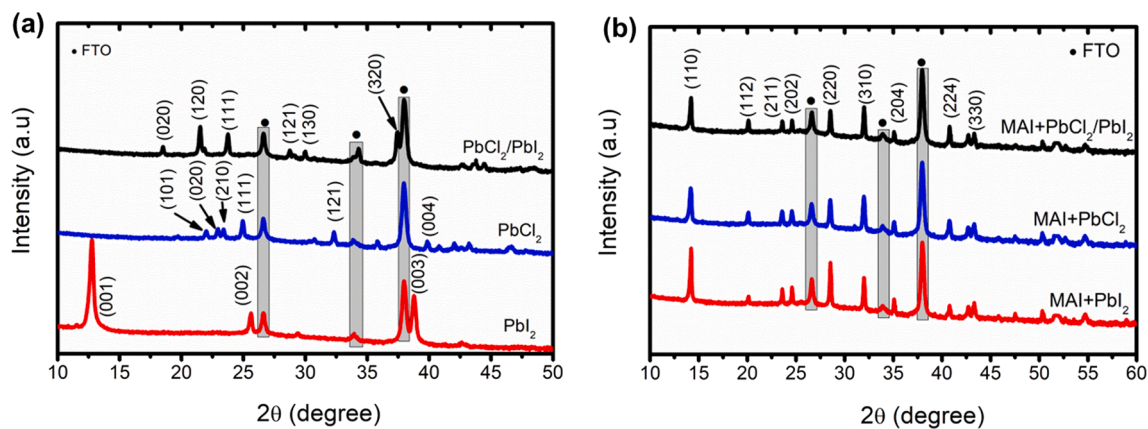


Fig. 2. (a) XRD patterns of lead halide films deposited in the first step(s). (b) XRD patterns of the converted perovskite films in the second/last step.

2017).

The double layered Pb halide film ( $\text{PbCl}_2/\text{PbI}_2$  sample) on the other hand showed a mixed halide phase of  $\text{PbICl}$  through the reaction of  $\text{PbCl}_2$  and  $\text{PbI}_2$ . This phase is shown by diffraction peaks at  $18.47^\circ$ ,  $21.51^\circ$ ,  $23.68^\circ$ ,  $28.70^\circ$ ,  $30.02^\circ$ , and  $37.41^\circ$  indexed to the (020), (120), (111), (121), (130), and (320) diffracting planes, Fig. 2a top XRD pattern. These diffraction peaks belong to the orthorhombic (Pnma)  $\text{PbICl}$  structure (JCPDS, data no. 73–0361) (Fan et al., 2017; Yanbo Li et al., 2015; Wu et al., 2015). These XRD patterns show a successful deposition of  $\text{PbI}_2$ ,  $\text{PbCl}_2$ , and  $\text{PbICl}$  phases with the low-pressure CVD method, providing a viable way of synthesizing Cl doped perovskite films. The absence of peaks belonging to  $\text{PbI}_2$  or  $\text{PbCl}_2$  on the XRD patterns of the  $\text{PbCl}_2/\text{PbI}_2$  sample proves the existence of a pure  $\text{PbICl}$  phase during an in-situ reaction of  $\text{PbCl}_2$  and  $\text{PbI}_2$  compounds.

These films were subsequently exposed to MAI vapor for the conversion to perovskite films as the last step of the procedure, depicted in Fig. 1 schematic. XRD patterns of the converted perovskite are shown in Fig. 2b for all the samples; the perovskite sample naming is extended by adding MAI in front of the sample name used for Pb halides. The patterns show the known peaks of the tetragonal hybrid perovskite structure with major peaks at  $14.05^\circ$ ,  $28.54^\circ$ , and  $31.98^\circ$  assigned to the (110), (220), and (310) planes, respectively (Baikie et al., 2013). Interestingly, the perovskite film converted from a  $\text{PbI}_2$  layer (sample MAI +  $\text{PbI}_2$ ) has intense (110) and (220) peaks compared to the Cl-doped perovskite samples (sample MAI +  $\text{PbCl}_2$  and MAI +  $\text{PbCl}_2/\text{PbI}_2$ ) as shown in Fig. 2b, and more clearly in Fig. S1a and b. The higher intensity of these peaks is due to the preference of crystals along these planes for the  $\text{PbI}_2$ -based perovskite sample. The intensity ratio of the (310) to the (220)

peak is enhanced for the Cl-doped perovskite samples, suggesting a reduced texture compared to the pure iodine sample which showed more pronounced texture i.e. low (310)/(220) peak ratio (Fig. S1b). This reduced texture on the Cl-doped perovskite films is a first proof of a chlorine inclusion in these samples (sample MAI +  $\text{PbCl}_2$  and MAI +  $\text{PbCl}_2/\text{PbI}_2$ ) as has been previously reported (Yanbo Li et al., 2015).

There were no impurities detected in these samples such as the  $\text{PbI}_2$  impurity at  $12.70^\circ$ , while  $\text{MAPbCl}_3$  normally appears at  $15.80^\circ$  for chlorine containing perovskites (Fan et al., 2017; P. Luo et al., 2015; Wittich et al., 2018). The absence of these unwanted impurities confirms a successful conversion of the pre-deposited Pb halide films to a high-quality perovskite phase through the low-pressure CVD technique. This also indicates that there is no phase segregation in these samples. There was no significant lattice reduction for the chlorine doped samples compared to the  $\text{PbI}_2$ -based sample which indicate a negligible Cl content for these films (Yunlong Li et al., 2015; Liu et al., 2018). Calculated lattice parameters of a tetragonal perovskite phase are shown in Table S1.

Fig. 3a–c shows the planar scanning electron microscopy (SEM) micrographs of the Pb halide films on FTO/c- $\text{TiO}_2$  substrates obtained during the low-pressure CVD process. There is a clear difference in morphologies of the Pb halides films based on the different deposition conditions. Sample  $\text{PbCl}_2/\text{PbI}_2$  where the  $\text{PbCl}_2$  film was deposited first followed by  $\text{PbI}_2$  showed rough columnar-like grains mixed with flatter grains and spaces in-between (Fig. 3a); the average grain size was calculated to be about  $93 \pm 22$  nm as given in Table 1. This difference in grain shape of the  $\text{PbICl}$  film is related to the distinct grain formation of the  $\text{PbI}_2$  and  $\text{PbCl}_2$  as also shown by these individual layers in Fig. 3b

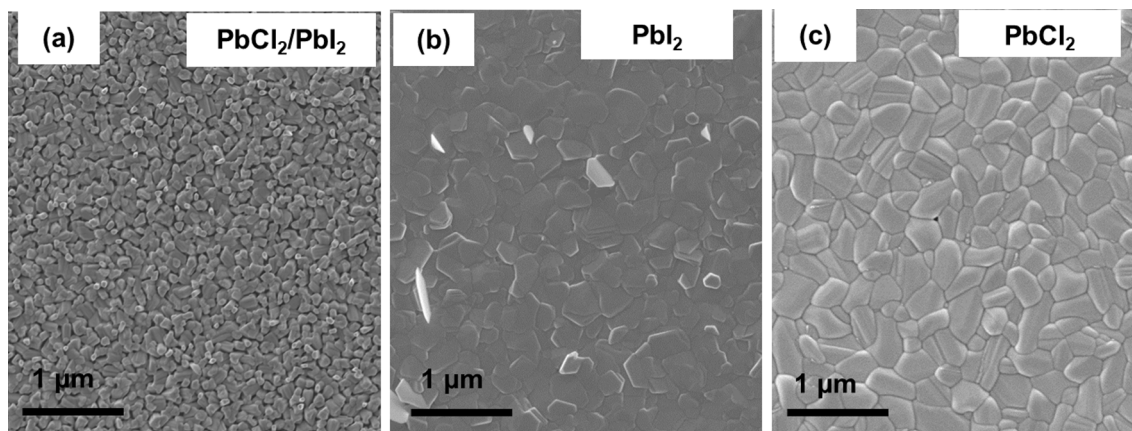


Fig. 3. Planar/surface SEM micrographs of pre-deposited lead halide films. (a) Sample  $\text{PbCl}_2/\text{PbI}_2$  ( $\text{PbICl}$  film), (b) Sample  $\text{PbI}_2$  ( $\text{PbI}_2$  film), and (c) Sample  $\text{PbCl}_2$  ( $\text{PbCl}_2$  film).

**Table 1**

Summary of Pb halides and perovskites film thicknesses, grain size, and Pb:I:Cl ratios obtained from EDS.

Sample name	Thickness (nm)	Grain size (nm)	Pb:I:Cl ratio (EDS)
PbCl <sub>2</sub> /PbI <sub>2</sub>	143 ± 6	93 ± 22	1 : 1.4 : 1.1
PbI <sub>2</sub>	150 ± 8	288 ± 86	1 : 2.6 : 0
PbCl <sub>2</sub>	150 ± 7	366 ± 89	1 : 0 : 2
MAI + PbCl <sub>2</sub> /PbI <sub>2</sub>	355 ± 5	578 ± 167	1 : 3.8 : 0
MAI + PbI <sub>2</sub>	295 ± 4	1048 ± 321	1 : 3.9 : 0
MAI + PbCl <sub>2</sub>	490 ± 6	937 ± 282	1 : 3.7 : 0

and c, respectively. PbI<sub>2</sub> grains form in a layer-by-layer pattern of hexagonal platelets (grains), evidenced by their flat morphology in Fig. 3b compared to the PbCl<sub>2</sub> film which forms more spherical, well defined grains as shown in Fig. 3c.

Starting with a film that has spherical grains (PbCl<sub>2</sub>), the subsequent second step resulted into PbI<sub>2</sub> platelets forming at different angles and interconnecting with the PbCl<sub>2</sub> grains, and finally after reacting, columnar PbICl grains were formed. This rough morphology of the PbICl phase was also identified by Fan et al. (2017) and suggested that it is beneficial for an easy conversion to perovskite. The PbI<sub>2</sub> film in Fig. 3b had smooth and flat grains with an average grain size of 288 ± 86 nm compared to the PbCl<sub>2</sub> counterpart which has larger and more spherical grains of about 366 ± 89 nm in average as seen in Fig. 3c. The smaller average grain size of the PbICl film is due to grain coarsening during the reaction of PbCl<sub>2</sub> and PbI<sub>2</sub> compounds. Grain size distribution of these Pb halides films is shown in Fig. S2a–c.

The planar/surface SEM micrographs of the converted perovskite films are shown in Fig. 4a–c depicting well-defined and compact grains, larger than those of the pre-deposited Pb halide counterparts. The perovskite film converted from the PbICl film (sample MAI + PbCl<sub>2</sub>/PbI<sub>2</sub>) shows smaller grains than the pure halide counterparts, but with larger than the grains of the starting PbICl layer as shown Fig. 4a. The average lateral grain size of this sample was estimated to be about 578 ±

167 nm, shown in Table 1. In contrast, sample MAI + PbI<sub>2</sub> showed very large, compact and flat grains with an average grain size of 1048 ± 321 nm even though there were grains larger than 2 μm as shown in Fig. 4b. On the other hand, sample MAI + PbCl<sub>2</sub> showed well-defined, compact and rougher grains with an average size of 937 ± 282 nm as illustrated in Fig. 4c. Another sample that was compared in this study was under conditions where a film of PbI<sub>2</sub> was deposited first followed by a PbCl<sub>2</sub> film, forming a PbICl phase that was eventually converted to a perovskite, yielding a similar morphology to the MAI + PbCl<sub>2</sub>/PbI<sub>2</sub> film (Fig. S3). The perovskite grain size distributions are also included in the supporting information, Fig. S4a–d.

The difference in grain sizes between these samples can be attributed to the morphology of the starting Pb halides layers. The PbICl films had very small and rough grains and this might have contributed to poor crystallization of the final perovskite film, with small grains of the starting Pb halide yielding smaller perovskite grains after conversion. The porosity of the starting PbICl film was shown to result into larger perovskite grains during solution method (Fan et al., 2017) but our results proves otherwise for low pressure CVD. Instead, the porous nature of the PbICl phase might have improved the conversion rate to perovskite but all these samples in this study were converted for 60 min as it was an optimum conversion time for PbI<sub>2</sub> and PbCl<sub>2</sub> films.

In comparison, the perovskite prepared from a PbCl<sub>2</sub> film had relatively larger grains compared to the sample MAI + PbCl<sub>2</sub>/PbI<sub>2</sub> due to larger grains of the starting PbCl<sub>2</sub>. The sample converted from a flat PbI<sub>2</sub> film had very large grains and this is due to easy intercalation of the MAI molecule into the layered structure of the PbI<sub>2</sub> (Ngqoloda et al., 2020b). These results contradict what have been previously reported that Cl incorporation into the perovskite structure improves crystallization leading to larger grains reported for perovskite films prepared by solution methods (Fan et al., 2017; Luo et al., 2015b; Tavakoli et al., 2015; Wittich et al., 2018). Our results further shows that low pressure CVD grown PbI<sub>2</sub> film leads to larger and smooth perovskite grains compared to starting with a Cl-containing compound.

The respective cross sectional SEM in Fig. 4d–f shows continuous

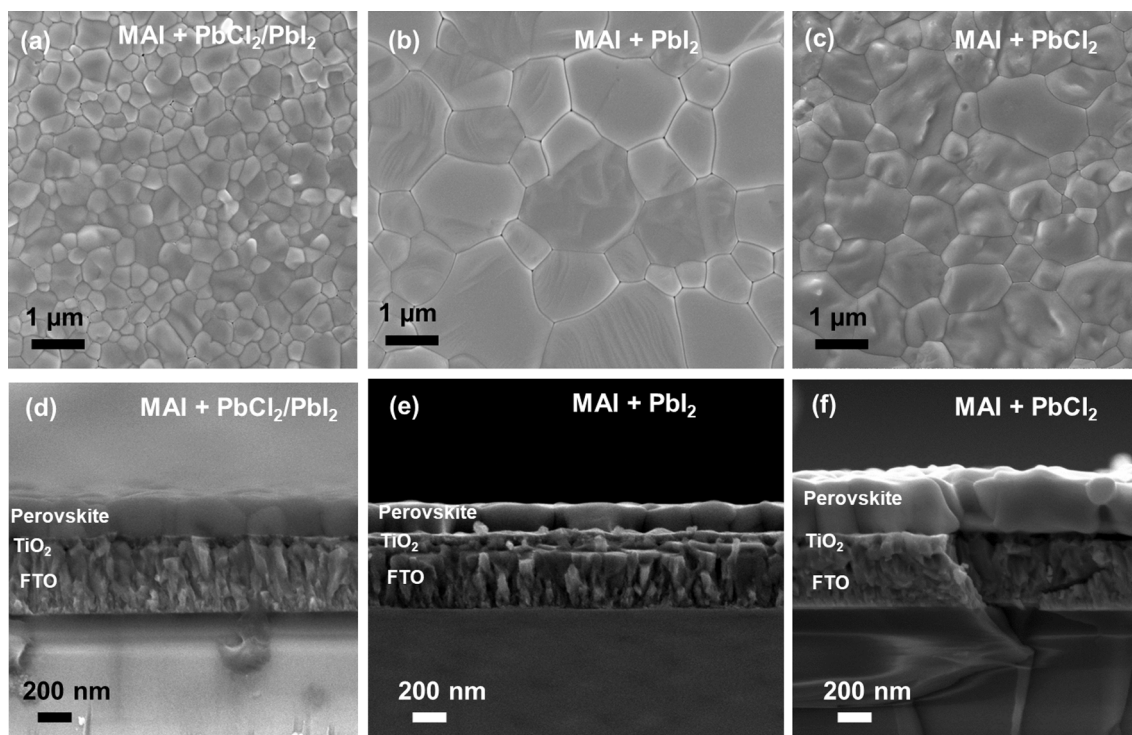


**Fig. 4.** (a–c) Planar/surface SEM micrographs of the converted perovskite thin films during the last step of the sequential CVD process with sample number as shown on the micrographs. (d–f) Cross sectional view SEM micrographs of the perovskite films in (a–c), respectively.

grains across the film thickness, which is an advantage for efficient charge transport as there are less grain boundaries and hence suppressed charge recombination in the device (Zhang et al., 2019). Further, these cross-sectional SEM micrographs also illustrate a perfect contact between the perovskite films and the underlying c-TiO<sub>2</sub> layer. These perovskite films have a uniform thickness over large areas (Fig. S5a–c) demonstrating a scalable advantage of employing the sequential CVD method. The perovskite film converted from the PbI<sub>2</sub> film had thickness of about 295 ± 4 nm (Fig. 4e), almost double that of the starting PbI<sub>2</sub> and thinner than the other two samples. Perovskite sample MAI + PbCl<sub>2</sub>/PbI<sub>2</sub> resulted in a thickness of 355 ± 5 nm (Fig. 4d) from about 143 nm starting PbI<sub>2</sub> film, and finally sample MAI + PbCl<sub>2</sub> had a thickness of 490 ± 6 nm (Fig. 4f) that is more than 3 times the starting PbCl<sub>2</sub> film.

The film thickness increase for these converted perovskites is consistent with the known volume expansion of Pb halide films when converted to perovskite phase (C.-W. Chen et al., 2014; Q. Chen et al., 2014; Ha et al., 2014; Leyden et al., 2014). Furthermore, the lateral grain size of these films are larger than the film thickness especially for sample MAI + PbI<sub>2</sub> and MAI + PbCl<sub>2</sub>, and this is also beneficial for better device performance compared to solution processed perovskites (Yanbo Li et al., 2015; Tavakoli et al., 2015). The summary of film thicknesses and grain sizes are provided in Table 1.

Energy dispersive X-ray spectroscopy (EDS) was employed to study elemental composition of both Pb halide films and the converted perovskite films. The summary of the atomic ratio of Pb/I/Cl is given in Table 1 for all the samples studied here. Firstly, there was more iodine detected in all the samples with Pb:I ratio of 1:2.6 for the PbI<sub>2</sub> which theoretically should be 1:2. The PbI<sub>2</sub> film had a Pb:I:Cl ratio of 1:1.7:1 and the PbCl<sub>2</sub> film had a Pb:Cl ratio of 1:2 agreeing well with the theoretical value of 1:2. These results were important in this study to

show that Cl ions remained in the PbI<sub>2</sub> films even though these films were formed under high temperatures and low pressures.

The converted perovskites on the other hand showed no Cl composition in the EDS analysis, which also confirms the limitation of EDS for detecting low atomic composition (detection limit of 0.1–1 atomic %) (Ono et al., 2017). The conversion to perovskites here was achieved at nominal substrate temperatures of 130 °C comparable to that of PbI<sub>2</sub> phase formation (125 °C). The Cl was not replaced by the iodine during PbI<sub>2</sub> phase formation, but this did occur during conversion to perovskite where no Cl could be detected. Comparing these two conditions it shows that the smaller ionic radii of Cl causes it to be easily replaced by larger ionic radii of iodine only during perovskite phase formation in the presence of methyl ammonium. This means the Cl ions on the perovskite structure are weakly bonded to the Pb whereas they are tightly bonded on the PbI<sub>2</sub> structure.

The formation of a perovskite phase with the presence of the MA molecule further facilitates the replacement of Cl ions by the iodine. The EDS results also show that the chlorine was completely replaced by iodine during conversion to perovskites, even when we started with the pure PbCl<sub>2</sub> film (sample MAI + PbCl<sub>2</sub>). To study the elemental composition in detail, X-ray photoelectron spectroscopy (XPS) was employed on the converted perovskite films. The XPS full survey spectra of the surface of the perovskite films are shown in Fig. 5a, showing the elements in the films (Yu et al., 2014). The absence of the Cl 2p peak between 196 eV and 202 eV (Fan et al., 2017; Yu et al., 2014) in the XPS spectra (Fig. 5b) confirms that Cl is not present in these perovskite films, which is in agreement with the EDS data. The possible scenario is that during the conversion of PbCl<sub>2</sub> or PbI<sub>2</sub> to the perovskite phase, these compounds dissociates and Cl<sup>-</sup> escapes in gaseous phase as MACl with Pb or iodine remaining in the perovskites (Kim et al., 2015; Zhang

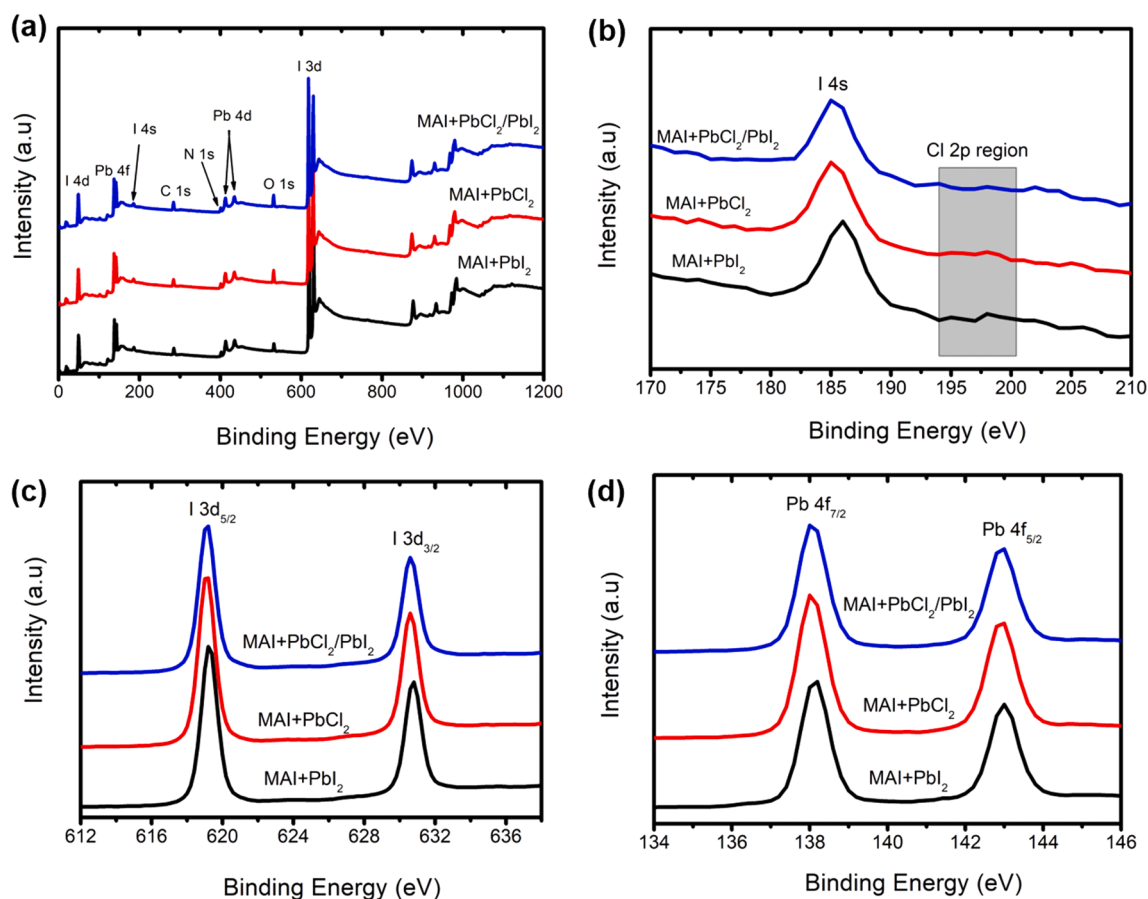


Fig. 5. (a) XPS full survey spectra of the top surface of converted perovskite films. (b) Zoomed XPS spectra from (a) showing the region of Cl 2p peak. (c, d) High resolution XPS core level spectra of I 3d, and Pb 4f, respectively.

et al., 2019).

Also shown in Fig. 5c and d are the high resolution XPS core level spectra of I 3d and Pb 4f, respectively, of the perovskite films. There are no observable shifts in peak positions for the I 3d and Pb 4f binding energies with respect to different samples, suggesting a similar chemical environment on all three perovskite samples. The similar binding energies for I 3d and Pb 4f in all these perovskites films is consistent with the absence of Cl in the films. Further, there is no indication of metallic lead ( $Pb^0$ ) in these perovskite samples (Fig. 5d), which usually has a small hump at about 137 eV and 141 eV binding energies that are associated with unbonded Pb (Kim et al., 2015; Zhang et al., 2015). The presence of  $Pb^0$  in the perovskites act as a defect site and therefore undesirable. Lastly, the calculated atomic composition from the high resolution XPS spectra of iodine and lead showed similar results to that of the EDS results. The Pb:I:Cl ratio from XPS were: 1:4.0:0 (sample MAI +  $PbI_2$ ), 1:3.9:0 (sample MAI +  $PbCl_2$ ), and 1:3.9:0 (sample MAI +  $PbCl_2/PbI_2$ ). Again, this excessive iodine content is consistent with the absence of unbonded metallic lead, which confirms the high quality perovskite films.

### 3.2. Optical properties and device characterization

The absorbance spectra of the converted perovskite films are all identical with high absorption over the visible range as shown in Fig. 6a. Sample MAI +  $PbCl_2$  showed a slightly higher absorbance in this region and this is attributed to the increased film thickness of this sample compared to the other two samples. Similar optical band gaps of 1.59 eV for all the samples was estimated by analyzing Tauc plots for a direct

band gap perovskite as shown in Fig. S6a (Yanbo Li et al., 2015). The estimated band gaps also lie within reported values of tetragonal  $MAPbI_3$  perovskites (Green et al., 2015; Lin et al., 2015) with no indication of a band gap shift for Cl doped perovskites compared to the pure iodine based counterparts (Chae et al., 2015; Liu et al., 2018). The absorbance spectra of the perovskites were also simulated near the band-edge using the Elliott model to extract the band gap and exciton binding energies, shown in Fig. S7. The band gap energies are almost the same for all three samples ranging between 1.70 eV and 1.72 eV; larger than the Tauc based band gaps as expected (Green et al., 2015). The excitonic binding energies of the three samples lie between 45 and 54 meV, further suggesting low trap densities for these perovskite samples.

The photoluminescence (PL) spectra of the perovskites films are shown in Fig. 6b, where an emission peak centered at about 777 nm (1.596 eV) is observed for the MAI +  $PbCl_2/PbI_2$  and MAI +  $PbI_2$  samples. The emission peak for the MAI +  $PbCl_2$  perovskites sample is centered at 773 (1.604 eV) nm displaying a slight blue shift (4 nm) compared to the other perovskite samples. These PL emission peaks are consistent with the Tauc plots for the band gap ( $\sim 1.60$  eV) and agrees with literature (Cao et al., 2018; Yanbo Li et al., 2015; Zhang et al., 2019). The slight blue shift of the MAI +  $PbCl_2$  sample may be due to the minute presence of the Cl, although it was not detected by XPS and EDS (Cao et al., 2018; Zhang et al., 2019).

The planar perovskite solar cell devices were completed by a deposition of a Spiro–MeOTAD layer which acts as a hole transport material (HTM), and finally a thin layer (100 nm) of silver metal (Ag) as a back contact was deposited. The complete device had Glass/FTO/c-TiO<sub>2</sub>/perovskite/Spiro–MeOTAD/Ag sequence. The deposition of the HTM

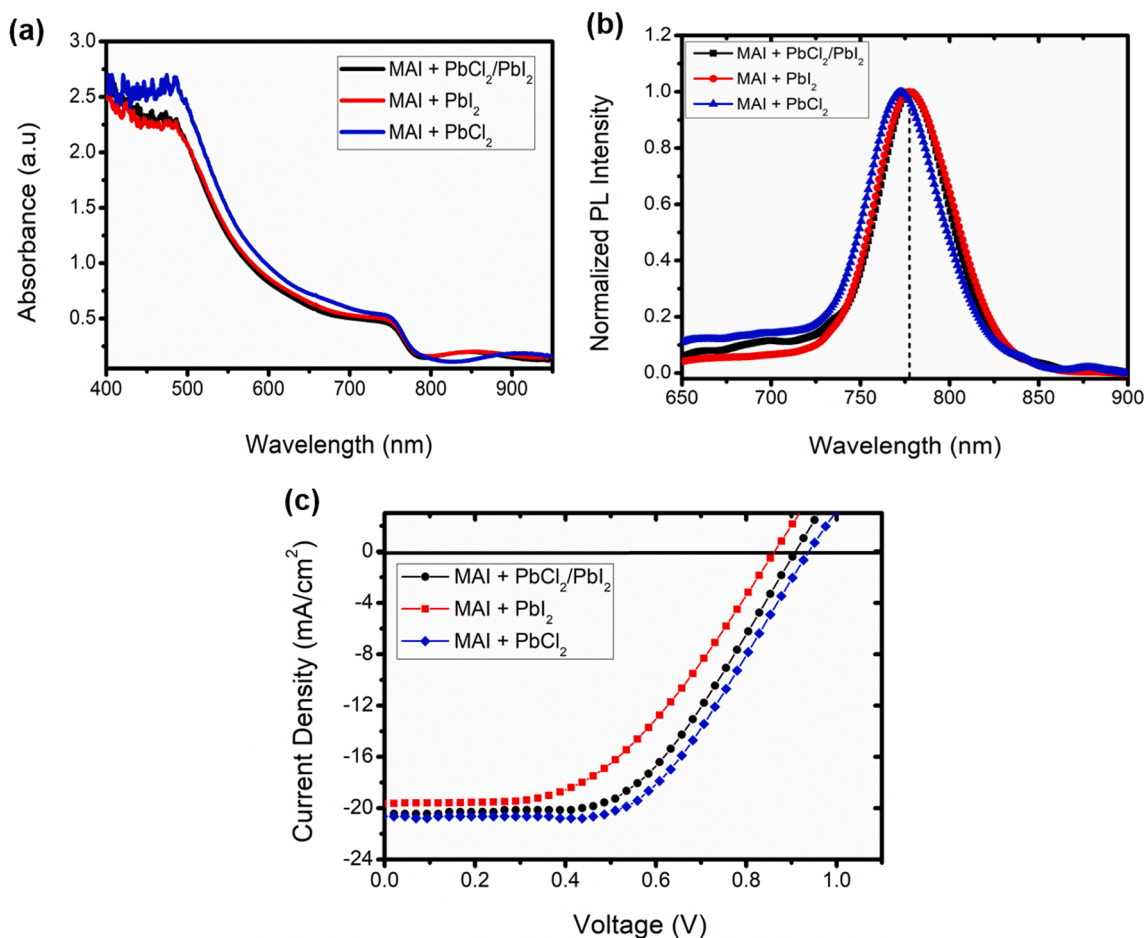


**Fig. 6.** (a) Absorbance spectrums of the converted perovskites films. (b) Normalized steady state PL spectra of the perovskites thin films on glass substrates (Glass/Perovskites). (c) J–V characteristic curves of the best perovskite solar cell devices under 100  $mW/cm^2$  illumination at reverse scan.

and the device characterization was done in ambient air (20 °C and 55% relative humidity) without any use of a glove box. The device performance was then characterized by measuring current and voltage under simulated AM 1.5G (100 mW/cm<sup>2</sup>) solar irradiation in ambient air. The current density–voltage (J–V) curves of all the samples are shown in Fig. 6c for reverse scan. Device parameters (best and average) are summarized in Table 2 with open circuit voltage ( $V_{oc}$ ), short circuit current density ( $J_{sc}$ ), fill factor (FF), and power conversion efficiency (PCE) provided. The forward scan J–V curves are shown in supporting information (Fig. S6b) and the parameters given in Table S2.

Interestingly, the chlorine doped perovskite devices showed well-improved  $V_{oc}$  of 0.907 V for sample MAI + PbCl<sub>2</sub>/PbI<sub>2</sub> and 0.938 V for sample MAI + PbCl<sub>2</sub> compared to the pure iodine based device (MAI + PbI<sub>2</sub>) with  $V_{oc}$  = 0.862 V (Fig. 6c). The Cl doped perovskite samples also showed improved fill factor with 0.545 for sample MAI + PbCl<sub>2</sub>/PbI<sub>2</sub> and 0.562 for sample MAI + PbCl<sub>2</sub> when compared to MAI + PbI<sub>2</sub> sample which has a fill factor of 0.517. The measured current density of these samples was 20.55 mA/cm<sup>2</sup> for sample MAI + PbCl<sub>2</sub>/PbI<sub>2</sub>, 20.64 mA/cm<sup>2</sup> for sample MAI + PbCl<sub>2</sub> and 19.65 mA/cm<sup>2</sup> for sample MAI + PbI<sub>2</sub> (Fig. 6c). The highest PCE of 10.87% was from the sample MAI + PbCl<sub>2</sub> followed by 10.14% for sample MAI + PbCl<sub>2</sub>/PbI<sub>2</sub>, and lastly 8.76% for sample MAI + PbI<sub>2</sub>. These devices had lower PCE compared to our previous publication (Ngqoloda et al., 2020b) and even worse for the MAI + PbI<sub>2</sub> sample. This was because the deposition conditions were altered for best optimum film conditions of the Cl-doped samples.

Since the MAI + PbI<sub>2</sub> sample had larger grains it is expected to have a reduced density of trap states at the grain boundaries compared to smaller grain size Cl-doped samples (Stewart et al., 2016; Zhao et al., 2016), which should ideally improve the device performance. However, this is contradictory to our observed results, which shows that the device performance is not solely dependent on the perovskite grain size. The low concentration of Cl present in the doped samples demonstrates that Cl passivates the dangling bond defects at grain boundaries and on the film surface, resulting in reduced charge trap states and the suppression of charge recombination (Stewart et al., 2016; Zhao et al., 2016). This leads to an improved charge injection towards the transport layers, leading to an increased  $V_{oc}$ , FF and ultimately their performance (Chen et al., 2015; Liu et al., 2018; Wu et al., 2019). In addition to this, the expected longer carrier diffusion length in the Cl-doped perovskite thin films plays a crucial role in improving the solar cell performance (Leyden et al., 2015). In general, these perovskite devices suffer from relatively poor fill factor and  $V_{oc}$  mainly due to poor charge transport at the perovskite/c-TiO<sub>2</sub> interface resulting in poor device performances (Ahn et al., 2016; Jena et al., 2015).

The forward scan J–V curves are shown in Fig. S6b and all showed poor FF compared to the reverse scans, which demonstrates high device hysteresis. Hysteresis is a norm in planar heterojunction perovskite devices that result from poor charge transport at the electron transport layer, i.e. compact TiO<sub>2</sub> (Ahn et al., 2016; Jena et al., 2015; Luo et al., 2015b). A similar trend was observed during the forward scans with higher  $V_{oc}$  for Cl doped perovskite films ( $V_{oc}$  higher than 0.9 V) compared to the PbI<sub>2</sub>-based perovskite device with  $V_{oc}$  = 0.791 V. These device performances prove that the incorporation of chlorine in the perovskite structure improves the performance of organic–inorganic perovskite solar cells. It is shown here that by starting with a pure PbCl<sub>2</sub> layer and its exposure to MAI vapor improves  $V_{oc}$  by 76 mV compared to the pure iodine-based counterparts.

#### 4. Conclusion

A low-pressure CVD method was used to successfully deposit Cl-doped perovskite solar cell devices via three- and two-step routes from chlorine-containing Pb halide films and compared to pure iodine-based perovskite. It is demonstrated here for the first time that Cl is not substituted by iodine during the high temperature sequential CVD of PbCl<sub>2</sub> and PbI<sub>2</sub> layers. Instead, the compounds reacted to form a stable

**Table 2**

Perovskite Solar cell device performances of different samples (4 devices each) extracted from the J–V curves.

Sample		$V_{oc}$ (V)	$J_{sc}$ (mA/cm <sup>2</sup> )	FF	PCE (%)
MAI + PbCl <sub>2</sub> /PbI <sub>2</sub>	Best	0.907	20.55	0.545	10.14
	Average	0.903 ± 0.012	19.52 ± 0.37	0.528 ± 0.009	9.57 ± 0.11
MAI + PbI <sub>2</sub>	Best	0.862	19.65	0.517	8.76
	Average	0.830 ± 0.02	18.45 ± 0.66	0.485 ± 0.016	7.43 ± 0.50
MAI + PbCl <sub>2</sub>	Best	0.938	20.64	0.562	10.87
	Average	0.936 ± 0.008	19.73 ± 0.46	0.536 ± 0.014	9.86 ± 0.42

lead chloride iodide phase. It is further shown that Cl is easily substituted by iodine during the perovskite formation under similar substrate temperatures as the Pb halide deposition, though different deposition pressures were used. We also showed that the presence of Cl in the Pb halide films does not necessarily improve the grain size of the final perovskite films compared to its pure iodine counterparts, but its presence is still beneficial to the device performance. Lastly, the open circuit voltage ( $V_{oc}$ ) was improved significantly for perovskites prepared from Cl-containing Pb halides, thereby increasing the device efficiencies. The highest device performance of 10.87% ( $V_{oc}$  = 0.938 V) was achieved for the perovskite converted from PbCl<sub>2</sub> and 10.14% ( $V_{oc}$  = 0.907 V) for the perovskite converted from the PbI<sub>2</sub> layer compared to just 8.76% ( $V_{oc}$  = 0.862 V) for PbI<sub>2</sub>-based perovskite. This improved  $V_{oc}$  and efficiency were attributed to the low trap density at grain boundaries and at film surface for Cl-doped perovskites allowing easy injection of charge carriers to the respective charge transport layers. This work will aid in the development of a scalable, low-cost synthesis technique for the manufacturing of mixed-halide hybrid perovskite solar panels.

#### Declaration of Competing Interest

The authors declare that they have no known competing financial interests or personal relationships that could have appeared to influence the work reported in this paper.

#### Acknowledgements

Financial support is gratefully acknowledged from the National Research Foundation (Grant No. 103621, 92520, and 93212); the NRF MANUS-MATSCI program; the ARMSCOR DESUP project; the University of the Western Cape; and the University of Missouri–University of Western Cape Linkage Program. SG was supported by the National Science Foundation Grant No. DMR-1807263.

#### Appendix A. Supplementary material

Supplementary data to this article can be found online at <https://doi.org/10.1016/j.solener.2020.12.042>.

#### References

- Ahn, N., Kwak, K., Jang, M.S., Yoon, H., Lee, B.Y., Lee, J.-K., Pikhitsa, P.V., Byun, J., Choi, M., 2016. Trapped charge-driven degradation of perovskite solar cells. *Nat. Commun.* 7, 13422. <https://doi.org/10.1038/ncomms13422>.
- Baikie, T., Fang, Y., Kadro, J.M., Schreyer, M., Wei, F., Mhaisalkar, S.G., Graetzel, M., White, T.J., 2013. Synthesis and crystal chemistry of the hybrid perovskite (CH<sub>3</sub>NH<sub>3</sub>)PbI<sub>3</sub> for solid-state sensitised solar cell applications. *J. Mater. Chem. A* 1, 5628. <https://doi.org/10.1039/c3ta10518k>.
- Best Research-Cell Efficiency Chart | Photovoltaic Research | NREL [WWW Document], n.d. URL <https://www.nrel.gov/pv/cell-efficiency.html> (accessed 9.16.20).
- Cao, X., Zhi, L., Jia, Y., Li, Y., Zhao, K., Cui, X., Ci, L., 2018. Enhanced efficiency of perovskite solar cells by introducing controlled chloride incorporation into MAPbI<sub>3</sub>

- perovskite films *Electrochimica Acta* Enhanced efficiency of perovskite solar cells by introducing controlled chloride incorporation into MAPbI<sub>3</sub>. *Electrochim. Acta* 275, 1–7. <https://doi.org/10.1016/j.electacta.2018.04.123>.
- Chae, J., Dong, Q., Huang, J., Centrone, A., 2015. Chlorine incorporation process in CH<sub>3</sub>NH<sub>3</sub>PbI<sub>3-x</sub>Cl<sub>x</sub> perovskites via nanoscale bandgap maps. *Nano Lett.* 15, 8114–8121. <https://doi.org/10.1021/acs.nanolett.5b03556>.
- Chen, C.-W., Kang, H.-W., Hsiao, S.-Y., Yang, P.-F., Chiang, K.-M., Lin, H.-W., 2014a. Efficient and uniform planar-type perovskite solar cells by simple sequential vacuum deposition. *Adv. Mater.* 26, 6647–6652. <https://doi.org/10.1002/adma.201402461>.
- Chen, Q., Zhou, H., Fang, Y., Stieg, A.Z., Song, T.-B., Wang, H.-H., Xu, X., Liu, Y., Lu, S., You, J., Sun, P., McKay, J., Goorsky, M.S., Yang, Y., 2015. The optoelectronic role of chlorine in CH<sub>3</sub>NH<sub>3</sub>PbI<sub>3</sub>(Cl)-based perovskite solar cells. *Nat. Commun.* 6, 7269. <https://doi.org/10.1038/ncomms8269>.
- Chen, Q., Zhou, H., Hong, Z., Luo, S., Duan, H.-S., Wang, H.-H., Liu, Y., Li, G., Yang, Y., 2014b. Planar heterojunction perovskite solar cells via vapor-assisted solution process. *J. Am. Chem. Soc.* 136, 622–625. <https://doi.org/10.1021/ja411509g>.
- Costa, J.C.S., Azevedo, J., Santos, L.M.N.B.F., Mendes, A., 2017. On the deposition of lead halide perovskite precursors by physical vapor method. *J. Phys. Chem. C* 121, 2080–2087. <https://doi.org/10.1021/acs.jpcc.6b11625>.
- Dong, Q., Yuan, Y., Shao, Y., Fang, Y., Wang, Q., Huang, J., 2015. Abnormal crystal growth in CH<sub>3</sub>NH<sub>3</sub>PbI<sub>3-x</sub>Cl<sub>x</sub> using a multi-cycle solution coating process. *Energy Environ. Sci.* 8, 2464–2470. <https://doi.org/10.1039/C5EE01179E>.
- Fan, L., Ding, Y., Luo, J., Shi, B., Yao, X., Wei, C., Zhang, D., Wang, G., Sheng, Y., Chen, Y., Hagfeldt, A., Zhao, Y., Zhang, X., 2017. Elucidating the role of chlorine in perovskite solar cells. *J. Mater. Chem. A* 5, 7423–7432. <https://doi.org/10.1039/C7TA00973A>.
- Green, M.A., Jiang, Y., Soufiani, A.M., Ho-Baillie, A., 2015. Optical properties of photovoltaic organic-inorganic lead halide perovskites. *J. Phys. Chem. Lett.* 6, 4774–4785. <https://doi.org/10.1021/acs.jpclett.5b01865>.
- Ha, S.T., Liu, X., Zhang, Q., Giovanni, D., Sum, T.C., Xiong, Q., 2014. Synthesis of organic-inorganic lead halide perovskite nanolayers: towards high-performance perovskite solar cells and optoelectronic devices. *Adv. Opt. Mater.* 2, 838–844. <https://doi.org/10.1002/adom.201400106>.
- Ioakeimidis, A., Christodoulou, C., Lux-Steiner, M., Fostiropoulos, K., 2016. Effect of PbI<sub>2</sub> deposition rate on two-step PVD/CVD all-vacuum prepared perovskite. *J. Solid State Chem.* 244, 20–24. <https://doi.org/10.1016/j.jssc.2016.08.034>.
- Jena, A.K., Chen, H.-W., Kogo, A., Sanehira, Y., Ikegami, M., Miyasaka, T., 2015. The interface between FTO and the TiO<sub>2</sub> compact layer can be one of the origins to hysteresis in planar heterojunction perovskite solar cells. *ACS Appl. Mater. Interfaces* 7, 9817–9823. <https://doi.org/10.1021/acsami.5b01789>.
- Jena, A.K., Kulkarni, A., Miyasaka, T., 2019. Halide perovskite photovoltaics: background, status, and future prospects. *Chem. Rev.* 119, 3036–3103. <https://doi.org/10.1021/acs.chemrev.8b00539>.
- Kim, T.G., Seo, S.W., Kwon, H., Hahn, J., Kim, J.W., 2015. Influence of halide precursor type and its composition on the electronic properties of vacuum deposited perovskite films. *Phys. Chem. Chem. Phys.* 17, 24342–24348. <https://doi.org/10.1039/C5CP04207K>.
- Kojima, A., Teshima, K., Shirai, Y., Miyasaka, T., 2009. Organometal halide perovskites as visible-light sensitizers for photovoltaic cells. *J. Am. Chem. Soc.* 131, 6050–6051. <https://doi.org/10.1021/ja809598r>.
- Leyden, M.R., Jiang, Y., Qi, Y., 2016. Chemical vapor deposition grown formamidinium perovskite solar modules with high steady state power and thermal stability. *J. Mater. Chem. A* 4, 13125–13132. <https://doi.org/10.1039/C6TA04267H>.
- Leyden, M.R., Lee, M.V., Raga, S.R., Qi, Y., 2015. Large formamidinium lead trihalide perovskite solar cells using chemical vapor deposition with high reproducibility and tunable chlorine concentrations. *J. Mater. Chem. A* 3, 16097–16103. <https://doi.org/10.1039/C5TA03577E>.
- Leyden, M.R., Ono, L.K., Raga, S.R., Kato, Y., Wang, S., Qi, Y., 2014. High performance perovskite solar cells by hybrid chemical vapor deposition. *J. Mater. Chem. A* 2, 18742–18745. <https://doi.org/10.1039/C4TA04385E>.
- Li, Y., Cooper, J.K., Buonsanti, R., Giannini, C., Liu, Y., Toma, F.M., Sharp, I.D., 2015a. Fabrication of planar heterojunction perovskite solar cells by controlled low-pressure vapor annealing. *J. Phys. Chem. Lett.* 6, 493–499. <https://doi.org/10.1021/jz502720a>.
- Li, Y., Sun, W., Yan, W., Ye, S., Peng, H., Liu, Z., Bian, Z., Huang, C., 2015b. High-performance planar solar cells based on CH<sub>3</sub>NH<sub>3</sub>PbI<sub>3-x</sub>Cl<sub>x</sub> perovskites with determined chlorine mole fraction. *Adv. Funct. Mater.* 25, 4867–4873. <https://doi.org/10.1002/adfm.201501289>.
- Lin, Q., Armin, A., Nagiri, R.C.R., Burn, P.L., Meredith, P., 2015. Electro-optics of perovskite solar cells. *Nat. Photonics* 9, 106–112. <https://doi.org/10.1038/nphoton.2014.284>.
- Liu, M., Johnston, M.B., Snath, H.J., 2013. Efficient planar heterojunction perovskite solar cells by vapour deposition. *Nature* 501, 395–398. <https://doi.org/10.1038/nature12509>.
- Liu, Z., Qiu, L., Juarez-Perez, E.J., Hawash, Z., Kim, T., Jiang, Y., Wu, Z., Raga, S.R., Ono, L.K., Liu, S., Qi, Y., 2018. Gas-solid reaction based over one-micrometer thick stable perovskite films for efficient solar cells and modules. *Nat. Commun.* 9, 3880. <https://doi.org/10.1038/s41467-018-06317-8>.
- Luo, P., Liu, Z., Xia, W., Yuan, C., Cheng, J., Lu, Y., 2015a. Uniform, stable, and efficient planar-heterojunction perovskite solar cells by facile low-pressure chemical vapor deposition under fully open-air conditions. *ACS Appl. Mater. Interfaces* 7, 2708–2714. <https://doi.org/10.1021/am5077588>.
- Luo, P., Liu, Z., Xia, W., Yuan, C., Cheng, J., Xu, C., Lu, Y., 2015b. Chlorine-conducted defect repairment and seed crystal-mediated vapor growth process for controllable preparation of efficient and stable perovskite solar cells. *J. Mater. Chem. A* 3, 22949–22959. <https://doi.org/10.1039/C5TA06813D>.
- Luo, S., You, P., Cai, G., Zhou, H., Yan, F., Daoud, W.A., 2016. The influence of chloride on interdiffusion method for perovskite solar cells. *Mater. Lett.* 169, 236–240. <https://doi.org/10.1016/j.matlet.2016.01.114>.
- Ng, T.-W., Chan, C.-Y., Lo, M.-F., Guan, Z.Q., Lee, C.-S., 2015. Formation chemistry of perovskites with mixed iodide/chloride content and the implications on charge transport properties. *J. Mater. Chem. A* 3, 9081–9085. <https://doi.org/10.1039/C4TA05819D>.
- Ngqoloda, S., Arendse, C.J., Muller, T.F., Cummings, F.R., Oliphant, C., 2020a. Effect of HTL thickness on air processed CVD perovskite solar cells. *Mater. Today Proc.* <https://doi.org/10.1016/j.matpr.2020.04.074>.
- Ngqoloda, S., Arendse, C.J., Muller, T.F., Miceli, P.F., Guha, S., Mostert, L., Oliphant, C. J., 2020b. Air-stable hybrid perovskite solar cell by sequential vapor deposition in a single reactor. *ACS Appl. Energy Mater.* 3, 2350–2359. <https://doi.org/10.1021/acsaem.9b01925>.
- Ono, L.K., Juarez-Perez, E.J., Qi, Y., 2017. Progress on perovskite materials and solar cells with mixed cations and halide anions. *ACS Appl. Mater. Interfaces* 9, 30197–30246. <https://doi.org/10.1021/acsaami.7b06001>.
- Ono, L.K., Leyden, M.R., Wang, S., Qi, Y., 2016. Organometal halide perovskite thin films and solar cells by vapor deposition. *J. Mater. Chem. A* 4, 6693–6713. <https://doi.org/10.1039/C5TA08963H>.
- Peng, Y., Jing, G., Cui, T., 2015. A hybrid physical-chemical deposition process at ultra-low temperatures for high-performance perovskite solar cells. *J. Mater. Chem. A* 3, 12436–12442. <https://doi.org/10.1039/C5TA01730K>.
- Richter, J.M., Abdi-Jalebi, M., Sadhanala, A., Tabachnyk, M., Rivett, J.P.H., Pazos-Outón, L.M., Gödel, K.C., Price, M., Deschler, F., Friend, R.H., 2016. Enhancing photoluminescence yields in lead halide perovskites by photon recycling and light out-coupling. *Nat. Commun.* 7, 13941. <https://doi.org/10.1038/ncomms13941>.
- Schieber, M., Zamoshchik, N., Khakhan, O., Zuck, A., 2008. Structural changes during vapor-phase deposition of polycrystalline-PbI<sub>2</sub> films. *J. Cryst. Growth* 310, 3168–3173. <https://doi.org/10.1016/j.jcrysgro.2008.02.030>.
- Shen, P.-S., Chen, J.-S., Chiang, Y.-H., Li, M.-H., Guo, T.-F., Chen, P., 2016a. Low-pressure hybrid chemical vapor growth for efficient perovskite solar cells and large-area module. *Adv. Mater. Interfaces* 3, 1500849. <https://doi.org/10.1002/admi.201500849>.
- Shen, P.-S., Chiang, Y.-H., Li, M.-H., Guo, T.-F., Chen, P., 2016b. Research Update: Hybrid organic-inorganic perovskite (HOIP) thin films and solar cells by vapor phase reaction. *APL Mater.* 4, 091509. <https://doi.org/10.1063/1.4962142>.
- Stewart, R.J., Grieco, C., Larsen, A.V., Doucette, G.S., Asbury, J.B., 2016. Molecular origins of defects in organohalide perovskites and their influence on charge carrier dynamics. *J. Phys. Chem. C* 120, 12392–12402. <https://doi.org/10.1021/acs.jpcc.6b03472>.
- Sun, H., Zhu, X., Yang, D., Yang, J., Gao, X., Li, X., 2014. Morphological and structural evolution during thermally physical vapor phase growth of PbI<sub>2</sub> polycrystalline thin films. *J. Cryst. Growth* 405, 29–34. <https://doi.org/10.1016/j.jcrysgro.2014.07.043>.
- Swartwout, R., Hoerantner, M.T., Bulović, V., 2019. Scalable deposition methods for large-area production of perovskite thin films. *Energy Environ. Mater.* 2, 119–145. <https://doi.org/10.1002/eem2.12043>.
- Tavakoli, M.M., Gu, L., Gao, Y., Reckmeier, C., He, J., Rogach, A.L., Yao, Y., Fan, Z., 2015. Fabrication of efficient planar perovskite solar cells using a one-step chemical vapor deposition method. *Sci. Rep.* 5, 14083. <https://doi.org/10.1038/srep14083>.
- Tombe, S., Adam, G., Heilbrunner, H., Apaydin, H., Iwuoha, E., Scherbar, M.C., 2017. Optical and electronic properties of mixed halide. *J. Mater. Chem. C* 5, 1714–1723. <https://doi.org/10.1039/C6TC04830G>.
- Tran, V.-D., Pammí, S.V.N., Dao, V.-D., Choi, H.-S., Yoon, S.-G., 2018. Chemical vapor deposition in fabrication of robust and highly efficient perovskite solar cells based on single-walled carbon nanotubes counter electrode. *J. Alloys Compd.* 747, 703–711. <https://doi.org/10.1016/j.jallcom.2018.02.006>.
- Wang, B., Chen, T., 2016. Exceptionally stable CH<sub>3</sub>NH<sub>3</sub>PbI<sub>3</sub> films in moderate humid environmental condition. *Adv. Sci.* 3, 1500262. <https://doi.org/10.1002/adv.201500262>.
- Wang, R., Mujahid, M., Duan, Y., Wang, Z.K., Xue, J., Yang, Y., 2019. A review of perovskite solar cell stability. *Adv. Funct. Mater.* 29. <https://doi.org/10.1002/adfm.201808843>.
- Williams, S.T., Zuo, F., Chueh, C.-C., Liao, C.-Y., Liang, P.-W., Jen, A.-K.-Y., 2014. Role of chloride in the morphological evolution of organo-lead halide perovskite thin films. *ACS Nano* 8, 10640–10654. <https://doi.org/10.1021/nn5041922>.
- Wittich, C., Mankel, E., Clemens, O., Lakus-Wollny, K., Mayer, T., Jaegermann, W., Kleebe, H.-J., 2018. Structural and compositional characteristics of vacuum deposited methylammonium lead halide perovskite layers in dependence on background pressure and substrate temperature. *Thin Solid Films* 650, 51–57. <https://doi.org/10.1016/j.tsf.2018.02.004>.
- Wu, N., Shi, C., Ying, C., Zhang, J., Wang, M., 2015. PbI<sub>2</sub>: A new precursor solution for efficient planar perovskite solar cell by vapor-assisted solution process. *Appl. Surf. Sci.* 357, 2372–2377. <https://doi.org/10.1016/j.apsusc.2015.09.254>.
- Wu, Y., Li, X., Fu, S., Wan, L., Fang, J., 2019. Efficient methylammonium lead trihalide perovskite solar cells with chloroformamidinium chloride (Cl-FACl) as an additive. *J. Mater. Chem. A* 7, 8078–8084. <https://doi.org/10.1039/C9TA01319A>.
- Yang, B., Brown, C.C., Huang, J., Collins, L., Sang, X., Unocic, R.R., Jesse, S., Kalinin, S. V., Belianinov, A., Jakowski, J., Geoghegan, D.B., Sumpter, B.G., Xiao, K., Ovchinnikova, O.S., 2017. Perovskites: Enhancing Ion Migration in Grain Boundaries of Hybrid Organic-Inorganic Perovskites by Chlorine (Adv. Funct. Mater. 26/2017). *Adv. Funct. Mater.* 27. <https://doi.org/10.1002/adfm.201770158>.
- Yang, B., Keum, J., Ovchinnikova, O.S., Belianinov, A., Chen, S., Du, M.-H., Ivanov, I.N., Rouleau, C.M., Geoghegan, D.B., Xiao, K., 2016. Deciphering halogen competition in organometallic halide perovskite growth. *J. Am. Chem. Soc.* 138, 5028–5035. <https://doi.org/10.1021/jacs.5b13254>.

- Yang, D., Yang, Z., Qin, W., Zhang, Y., Liu (Frank), S., Li, C., 2015. Alternating precursor layer deposition for highly stable perovskite films towards efficient solar cells using vacuum deposition. *J. Mater. Chem. A* 3, 9401–9405. <https://doi.org/10.1039/C5TA01824B>.
- Yu, H., Wang, F., Xie, F., Li, W., Chen, J., Zhao, N., 2014. The role of chlorine in the formation process of “CH<sub>3</sub>NH<sub>3</sub>PbI<sub>3-x</sub>Cl<sub>x</sub>” perovskite. *Adv. Funct. Mater.* <https://doi.org/10.1002/adfm.201401872> n/a-n/a.
- Zhang, H., Lv, Y., Wang, J., Ma, H., Sun, Z., Huang, W., 2019. Influence of Cl incorporation in perovskite precursor on the crystal growth and storage stability of perovskite solar cells. *ACS Appl. Mater. Interfaces* 11, 6022–6030. <https://doi.org/10.1021/acsami.8b19390>.
- Zhang, W., Pathak, S., Sakai, N., Stergiopoulos, T., Nayak, P.K., Noel, N.K., Haghighirad, A.A., Burlakov, V.M., DeQuilettes, D.W., Sadhanala, A., Li, W., Wang, L., Ginger, D.S., Friend, R.H., Snaith, H.J., 2015. Enhanced optoelectronic quality of perovskite thin films with hypophosphorous acid for planar heterojunction solar cells. *Nat. Commun.* 6, 10030. <https://doi.org/10.1038/ncomms10030>.
- Zhao, T., Chueh, C.-C., Chen, Q., Rajagopal, A., Jen, A.K.-Y., 2016. Defect passivation of organic-inorganic hybrid perovskites by diammonium iodide toward high-performance photovoltaic devices. *ACS Energy Lett.* 1, 757–763. <https://doi.org/10.1021/acsenergylett.6b00327>.